

JAMES Journal of Advances in Modeling Earth Systems*



RESEARCH ARTICLE

10.1029/2023MS003980

Key Points:

- "Showers" produce intense but localized rainfall; "rains" are weaker but widespread, producing more average precipitation
- Rains occur in very moist environments with weak instability while showers favor drier but more unstable environments
- Showers are associated with periodic bursts of rain in numerical simulations, rains produce continuous precipitation

Correspondence to:

D. J. Raymond, david.raymond@nmt.edu

Citation:

Raymond, D. J., Stone, Ž., & Sentić, S. (2024). Rains and showers in OTREC; weak temperature gradient modeling *Journal of Advances in Modeling Earth Systems*, 16, e2023MS003980. https://doi.org/10.1029/2023MS003980

Received 21 AUG 2023 Accepted 25 FEB 2024

Author Contributions:

Data curation: S. Sentić

Conceptualization: Ž. Stone

Funding acquisition: Ž. Stone Methodology: Ž. Stone, S. Sentić Software: S. Sentić Validation: Ž. Stone Writing – review & editing: Ž. Stone, S. Sentić

© 2024 The Authors. Journal of Advances in Modeling Earth Systems published by Wiley Periodicals LLC on behalf of American Geophysical Union.

This is an open access article under the terms of the Creative Commons Attribution-NonCommercial-NoDerivs License, which permits use and distribution in any medium, provided the original work is properly cited, the use is non-commercial and no modifications or

adaptations are made.

Rains and Showers in OTREC; Weak Temperature Gradient Modeling

D. J. Raymond¹, Ž. Stone¹, and S. Sentić¹

¹Physics Department and Climate and Weather Consortium, New Mexico Tech, Socorro, NM, USA

Abstract Rainfall in the tropics has been shown to be produced either by isolated but intense convective systems (*showers* regime) or widespread but weaker systems (*rains* regime). We examine significant rainfall systems observed in the OTREC project (Organization of Tropical East Pacific Convection) in order to tease out the physical mechanisms differentiating these two regimes. We find that rains occur in very moist environments, typically with weak conditional instability. In contrast, showers develop in drier environments with larger instability. Spectral weak temperature gradient numerical calculations show that showers are associated with episodic rainfall separated by significant quiescent periods, whereas rains produce continuous simulated rainfall after a spinup period. Mass flux profiles of showers and rains are very different, resulting in different effects on the large scale environment.

Plain Language Summary Rain can occur in intense bursts (*showers*) or in extended periods of less intense rainfall (*rains*). The latter regime often produces more total rain than the former. Using observations obtained over the tropical east Pacific and the southwest Caribbean, we have isolated the atmospheric conditions that occur for each of these rainfall regimes. In particular, rains require a very moist atmosphere but can occur with weak atmospheric instability, whereas showers occur in drier atmospheres but require stronger instability. Numerical simulations of rainfall systems confirm these results and reproduce the intense bursts of rain in showers versus the steady but weaker rainfall in rains.

1. Introduction

"...most [monsoon] rain falls in one of these two circumstances: either from (1) deep nimbostratus with embedded cumulonimbus when vertical wind shear and lower tropospheric convergence both are large (although rain intensity may fluctuate considerably, skies remain predominantly overcast), or (2) scattered towering cumulus or cumulonimbus, when vertical shear and lower tropospheric convergence both are small. I shall assign the term *rains* to the former and *showers* to the latter, realizing of course that sharp demarcation is impossible."

Thus does Colin Ramage introduce the topic of monsoon rainfall in his book on monsoon meteorology (Ramage, 1971) (Referred to hereafter as Ramage). He goes on to note that rains are associated with cloudy, near-moist-adiabatic soundings while showers occur in more unstable environments with clear air.

The distinction between rains and showers has been noted subsequently, though using different terminology. Williams et al. (1992), working in Northern Australia emphasized a similar bifurcation in convection, associating rains with active monsoon troughs and showers with monsoon breaks. They further noted that convective available potential energy (CAPE), surface wet bulb temperature, radar reflectivities, and lightning flash rates were higher in showers, but that integrated rainfall totals were larger in rains.

The observations of Ramage and Williams et al. (1992) were primarily over land. However the ship-based soundings and Doppler radar observations of convection in easterly waves in the tropical East Pacific of Petersen et al. (2003) show showers west of the wave trough and rains to the east by the criteria of Ramage. Thus Ramage's categorization of convection in the tropics appears to be valid over the ocean in this case.

Using composited satellite observations, Inoue and Back (2015a, 2015b, 2017), and Masunaga and L'Ecuyer (2014) inferred that at least some tropical deep convective systems over oceans undergo growing, mature, and decaying phases, much like that seen in isolated deep convective cells (Byers & Braham, 1948), but with much longer and somewhat variable time scales. Houze (2004) showed that the life cycle of such systems scales with the size of the system. These systems begin with bottom-heavy vertical mass flux profiles and progress

RAYMOND ET AL. 1 of 16



Journal of Advances in Modeling Earth Systems

10.1029/2023MS003980

to top-heavy, stratiform-like structure with corresponding changes in the vertically integrated convergence of moisture and divergence of moist entropy (or moist static energy). System evolution can be plotted as a series of points on the so-called gross moist stability (GMS) plane with moisture convergence (or dry static energy divergence) on the horizontal axis and moist entropy (or moist static energy) divergence on the vertical axis. The slope of the line passing through the origin and a particular point on this plot is the instantaneous GMS of the system at that time.

Given the limitations of satellite-based observations, in situ measurements are needed to answer many questions about oceanic convective systems. For instance, Houze et al. (2015) indicate that their convective classification algorithm may mis-identify some broad regions of shallow convective cells as deep stratiform regions.

The rains-showers dichotomy is not to be confused with the categorization of convective versus stratiform precipitation. Stratiform is actually the late phase of showers convection. As we shall see, rains typically lack the classic deep stratiform stage identified by Houze (1981) and others.

There have been numerous field programs studying tropical oceanic convection, for example, The Line Islands Experiment (Zipser, 1970), GATE (Houze & Betts, 1981), MONEX (Johnson & Chang, 2007), TOGA COARE (Webster & Lukas, 1992), EPIC2001 (Raymond et al., 2004), TCS08 (Elsberry & Harr, 2008), PREDICT (Montgomery et al., 2012), etc. These projects generally carried out case studies on targets of opportunity, and in so-doing obtained a great deal of information about the structure and evolution of the targeted systems.

The OTREC project (Organization of Tropical East Pacific Convection; August–September 2019) took a different approach. Systematic observations were made many times over pre-specified regions and randomly selected dates, at the same time each day, capturing snapshots of all convection as well as clear air conditions that occurred during these observational periods. Thus, an unbiased sample (except for the diurnal cycle) of convection in a particular season was obtained for each of the specified regions, which include the Pacific coastal region off of Colombia, the far southwest Caribbean, and the Intertropical Convergence Zone southwest of Costa Rica.

OTREC used the National Science Foundation, National Center for Atmospheric Research (NSF/NCAR) Gulfstream-V aircraft to deploy dropsondes with approximate 1° grid spacing. Dropsondes were launched from near 13 km, encompassing nearly the full depth of most convection in the region. They were then subjected to a three-dimensional variational analysis (3DVar) that provided regular grids of wind and thermodynamic data, from which various analyses were made (Fuchs-Stone et al., 2020; Raymond & Fuchs-Stone, 2021a). These analyses are used in this paper. In addition, the HIAPER Cloud Radar (HCR) (Vivekanandan et al., 2015), a W-band, downward-pointing, Doppler radar was used to document the characteristics of precipitation below the aircraft.

The 3DVar analysis allowed us to measure vertical mass flux (air density times the vertical velocity) on the 1° scale. This variable measures ascent and descent, with ascent generally strongest in regions of moist convection and rainfall. Dry vertical motions in the atmosphere tend to be oscillatory and are expected to largely cancel out with the horizontal averaging implicit in the 3DVar analysis. The relatively small values of vertical mass flux seen in regions away from convection support this hypothesis. The 3DVar analysis also allowed us to compute the distribution of vertically integrated moisture convergence and moist entropy divergence, and hence a snapshot of the GMS associated with observed convective systems.

Fuchs-Stone et al. (2020) found that vertical mass flux profiles in regions of actively growing or mature convection tended mostly to be bottom-heavy, that is, with maximum mass flux in the 2–4 km height range. This is roughly consistent with other evidence (Back & Bretherton, 2009a, 2009b; Back et al., 2017). However, regions with decaying convection exhibited typical top-heavy stratiform rain profiles, that is, with upward motion in the upper troposphere and descent in the lower troposphere (Byers & Braham, 1948; Houze, 1981, 1997; Mapes & Houze, 1993, 1995; Zipser, 1969). Raymond and Fuchs-Stone (2021a) further found that the integrated moisture convergence, and hence precipitation, attained peak values for large environmental saturation fraction, a kind of column relative humidity, and small instability index, a measure of low to mid-tropospheric moist convective instability. Sentic et al. (2022) showed that inclusion of OTREC dropsondes had a significant effect on ECMWF model analysis during the development of an East Pacific tropical cyclone.

Raymond and Fuchs-Stone (2021b) introduced a new convective model that implements the spectral weak temperature gradient (SWTG) assumption developed by Herman and Raymond (2014) and Wang et al. (2015).

RAYMOND ET AL. 2 of 16



Journal of Advances in Modeling Earth Systems

10.1029/2023MS003980

SWTG is a useful tool for studying tropical convection because it provides a realistic and efficient way of parameterizing the interaction between convection and the surrounding tropical environment. In particular, it assumes that the gravity waves emitted laterally in the adjustment toward horizontally homogeneous air density can be decomposed by vertical wavenumber, with the horizontal group velocity of each mode (equal to the phase speed for no rotation) set equal to that predicted by linear, hydrostatic dynamics. The sum of these gravity waves implies a mean vertical velocity in the convective region, called the weak temperature gradient vertical velocity. Mass continuity with this vertical flow further implies entrainment and detrainment of air to and from the surrounding environment.

Wang et al. (2015) developed a similar model, but with gravity wave vertical mode structure that takes into account the vertical structure of static stability rather than assuming constant stability with height. For the sake of simplicity, we retain the constant stability assumption. Raymond and Fuchs-Stone (2021b) found that the strongest modeled convection occurred in the OTREC region for the largest values of the saturation fraction, in agreement with observations.

In this paper we show that SWTG modeling successfully reproduces the vertical mass flux profiles for a large fraction of observed convective cases in OTREC. We then use the results of this modeling along with observations to see whether Ramage's rains-showers paradigm applies in the OTREC region and to determine how the Masunaga-Inoue-Back picture of convective life cycle works in this region. Since observations obtain only snapshots, we use the SWTG model to understand convective life cycles in the different cases. SWTG modeling in fact does appear to provide useful insight into time-dependent behavior of OTREC convection. From this we infer that pulsating or oscillatory behavior occurs in only some of the observed convective systems. In particular, we find that this behavior is strongest in Ramage's showers regime, whereas convection in the rains regime has a smaller tendency to oscillate. Pulsed convection tends to occur in simulations for drier initial soundings with greater moist convective instability and high elevations of maximum moist adiabatically lifted parcel buoyancy, whereas steady simulated convection is favored by moister, more stable soundings.

The combination of observations and SWTG numerical modeling shows that Ramage's categorization of tropical precipitation into showers and rains reveals a fundamental bifurcation in the dynamics of mesoscale convective systems dependent on differences in the convective environment. In particular, large instability and low humidity produce short-lived but intense showers, while smaller instability and higher humidity produce weaker but long-lasting rainfall. The former are characterized by rapid evolution from strong convective cells to stratiform rain, well characterized by their evolution in the gross most stability plane. The latter produce weaker convective cells which also form and decay, but do not result in the formation of strong cold pools and deep stratiform systems. Little evolution in the GMS plane is seen and rains systems tend to be associated with nearly zero GMS. Mass flux profiles of showers tend to evolve from bottom heavy to top heavy while rains typically maintain bottom heavy profiles through their life cycles. Thus, showers and rains have very different effects on the large scale flows in which they are embedded.

Section 2 describes how convective systems are selected for study and compiles their characteristics. The configuration of the SWTG model is also presented. Section 3 presents the results of simulations of the selected systems and compares them with observations. Section 4 summarizes the evidence linking pulsed and steady convection in the simulations to Ramage's showers and rains regimes respectively, and demonstrates how the characteristics of initial soundings determine which regime occurs. Section 5 presents the conclusions.

2. Methods

2.1. OTREC Data Set

We begin by defining thermodynamic parameters that are used in this paper. Raymond et al. (2003) introduced the deep convective inhibition (DCIN)

$$DCIN = s_{th}^* - s_{bl} \tag{1}$$

where s_{bl} is the average moist entropy in the lowest kilometer and s_{th}^* is the saturated moist entropy at a threshold level, defined here as the average value over 1.5–2 km elevation (The moist entropy is related closely to the

RAYMOND ET AL. 3 of 16

 Table 1

 Location, Time, Environmental and System Characteristics, and Stage of Development of Selected Convective Systems

Location, Time, Environmental and System Characteristics, and Stage of Development of Selected Convective Systems												
Date	Time	Lon	Lat	SST	II	SF	DCIN	CAPE	ZMAX	Sm	Se	Stage
0807-1	58.0	-88.5	8.5	28.0	18.2	0.85	14.8	335		-1,605	-77	d
0811-1	50.9	-78.0	5.0	26.8	21.8	0.84	-15.2	1,490		811	-229	d
0811-2	52.8	-80.0	6.0	26.9	24.9	0.86	-2.7	1,530	8	357	366	m
0812-1	56.2	-86.5	7.8	27.7	13.3	0.81	-1.5	1,061	8	1,614	-336	g
0812-2	57.7	-87.5	8.0	28.2	11.6	0.79	2.3	685	8	1,470	-176	g
0816-1	54.0	-78.5	6.3	26.9	3.8	0.91	-2.9	294	4	3,574	744	m
0816-2	63.3	-82.0	10.5	28.8	21.0	0.83	1.7	701	5	2,409	208	g
0822-1	64.9	-81.0	11.0	28.7	28.3	0.71	-4.7	2,432	8	2,121	- 5	m
0823-1	52.0	-88.5	4.5	27.4	9.7	0.79	-0.7	1,036	10	1,424	-444	g
0825-1	56.1	-79.0	7.0	27.1	34.7	0.78	22.3	626		-1,201	385	d
0903-1	56.5	-82.0	10.0	28.7	14.2	0.84	-4.0	1,117	4	1,952	102	m
0904-1	53.9	-89.0	6.0	28.1	10.3	0.87	-4.5	801	5	4,253	-352	g
0909-1	68.0	-78.5	5.5	27.2	23.4	0.83	-4.6	1,600	7	1,103	-340	g/d
0917-1	60.5	-79.5	5.8	26.8	10.2	0.89	-6.7	829	4	4,275	159	m
0921-1	58.0	-87.0	8.5	28.2	7.9	0.89	-13.2	1,386	4	4,138	-225	g
0921-2	63.6	-89.0	11.0	28.9	18.9	0.82	6.1	641		-188	507	d
0922-1	52.4	-79.5	6.5	27.3	18.8	0.90	-4.3	1,214	5	1,364	-254	m
0924-1	59.4	-87.5	9.5	28.3	35.5	0.79	9.1	1,381		-982	715	d
0925-1	49.5	-80.2	7.0	27.7	16.8	0.90	-9.5	1,327	5	6,389	-658	g
0927-1	51.2	-86.0	4.8	26.1	5.1	0.88	-1.1	417	8	2,436	-395	g
0927-2	61.5	-87.5	10.8	28.9	11.8	0.85	-9.3	1,108	7	4,627	-104	g
0928-1	58.6	-87.0	5.5	26.3	9.2	0.85	0.9	404	5	2,317	162	m
0928-2	64.2	-87.0	9.2	28.8	20.4	0.86	6.4	707		-165	569	d
0928-3	67.1	-87.5	11.0	29.0	10.5	0.89	2.2	377	4	3,478	823	m
0930-2	49.0	-88.0	4.0	26.6	18.1	0.82	-10.0	1,345	7	4,977	-395	m
1001-1	58.1	-87.7	8.0	27.3	10.5	0.81	-6.4	1,085	4	2,095	136	m
1002-1	56.2	-88.0	11.0	28.6	20.5	0.81	4.6	769		-93	115	d

Note. Date has the format (mmdd-case). Units are (ks UTC) for time, degrees for longitude and latitude, degrees Celsius for sea surface temperature SST, (J/K/kg) for instability index II and deep convective inhibition DCIN, (J/kg) for convective available potential energy CAPE, and (km) for the level of maximum lifted parcel buoyancy ZMAX. SF is dimensionless while Sm and Se have units of (W/m²). The letter "g" for Stage indicates "growing," "m" indicates "mature," and "d" indicates "decaying." The Case 0909-1 was a decaying system with convective redevelopment underneath. Decaying cases are omitted for ZMAX.

equivalent potential temperature. See the appendix in Raymond and Fuchs-Stone (2021b) for a formal definition.).

Ramage recognized tropospheric relative humidity as an important governing factor for convection, a conclusion reinforced by the results of Bretherton et al. (2004), Fuchs and Raymond (2002), Gjorgjievska and Raymond (2014), Raymond and Fuchs (2007), Sherwood (1999), and Sobel et al. (2004) and many others. The saturation fraction (denoted column relative humidity by Bretherton et al. (2004)) is an integrated measure of tropospheric relative humidity and is defined

$$SF = \int rdp / \int r^*dp \tag{2}$$

RAYMOND ET AL. 4 of 16

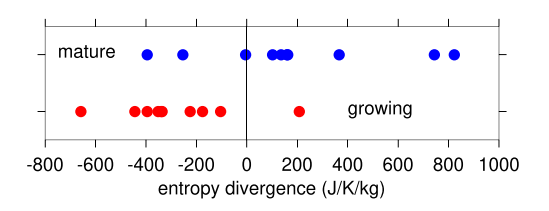


Figure 1. Entropy divergence calculated for growing (red dots) and mature (blue dots) convective systems as listed in Table 1.

where r and r^* are respectively the mixing ratio and the saturation mixing ratio, integrated in pressure over the troposphere.

The instability index

$$II = s_{lo}^* - s_{hi}^* \tag{3}$$

19422466, 2024, 3, Downloaded from https://agupubs.onlinelibrary.wiley.com/doi/10.1029/2023MS003980, Wiley Online Library on [22/03/2025]. See the Terms and Condit

is a measure of low to mid-tropospheric moist convective instability. The quantities s_{lo}^* and s_{hi}^* are respectively the saturated moist entropy averaged over 1–3 km and 5–7 km.

We approximate the CAPE by the equation

CAPE =
$$\int \left[s_{env}^*(z) - s_{bl} \right] \frac{\partial T}{\partial z} dz$$
 (4)

where the integral extends through the troposphere and the integrand is set to zero where it is negative. The quantity $s_{env}^*(z)$ is the environmental profile of saturated moist entropy and s_{bl} is the mean moist entropy in the lowest kilometer as in Equation 1. Another parameter characterizing the sounding is the level of maximum buoyancy of a lifted parcel, defined as the level of minimum saturated moist entropy, ZMAX.

A measure of the degree of top-heaviness or bottom-heaviness of the vertical mass flux profile is given by the equation

$$MFDIF = M_{hi} - M_{lo} \tag{5}$$

where M_{hi} and M_{lo} are respectively the mean mass fluxes in the intervals [7,9] km and [3,5] km.

Two additional variables of considerable importance were derived from the 3DVar analysis, the vertically integrated moisture convergence

$$Sm = -L \int \nabla_h \cdot (\mathbf{v}_h r) \rho dz \tag{6}$$

and the vertically integrated moist entropy divergence

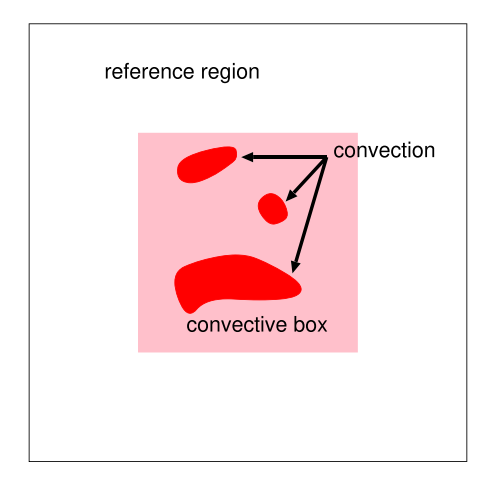


Figure 2. Schematic of spectral weak temperature gradient model domains. Conditions in the convective box control the convection while the convection itself and flows to and from the reference region control the convective box

$$Se = T_R \int \nabla_h \cdot (\mathbf{v}_h s) \rho dz \tag{7}$$

where \mathbf{v}_h is the horizontal wind, r is the mixing ratio, s is the specific moist entropy, and ρ is the density. The moisture convergence and entropy divergence are respectively multiplied by normalization factors $L = 2.5 \times 10^6$ J/kg and $T_R = 273.15$ K to convert them to units of watts per square meter. The normalized GMS (Raymond et al., 2009) is given by

$$NGMS = Se/Sm. (8)$$

We now describe how convection was analyzed in the OTREC data set. Infrared (IR) satellite loops with 2 km resolution were used to pick out the longitude and latitude of all significant convective events that were covered by Gulfstream-V dropsonde observations. These largely coincide with those found by Fuchs-Stone et al. (2020), though on occasion multiple events were selected in a single mission as warranted, which added to the list of candidate events. Table 1 shows the date, time, location, and parameter values taken from the 3DVar analysis at the specified longitude and latitude.

RAYMOND ET AL. 5 of 16

19422466, 2024, 3, Downloaded from https://agupubs.onlinelibrary.wiley.com/doi/10.1029/2023MS003980, Wiley Online Library on [22/03/2025]. See the Terms and Conditions (https://onlinelibrary.wiley.com/erms

-and-conditions) on Wiley Online Library for rules of use; OA articles are governed by the applicable Creative Commons Licenso

 Table 2

 Simulation Characteristics for Growing and Mature Cases

Date	Stage	Steady/Pulsed	Quality	Comment
0811-2	m	Single	Poor	Convection only in single pulse
0812-1	g	Pulsed	Fair	Best match in early transient
0812-2	g	Pulsed	Fair	Best match in early transient
0816-1	m	Steady	Good	
0816-2	g	Steady	Poor	
0822-1	m	Single	Poor	Convection only after initialization
0823-1	g	Pulsed	Good	Best match in early transient
0903-1	m	Steady	Good	
0904-1	g	Steady	Good	Best match in early transient
0909-1	g/d	Pulsed	Good	Matches in lower troposphere
0917-1	m	Steady	Good	
0921-1	g	Steady	Good	Best match in early transient
0922-1	m	Steady	Poor	
0925-1	g	Steady	Good	Best match in early transient
0927-1	g	Steady	Good	Best match in early transient
0927-2	g	Steady	Fair	Best match in early transient
0928-1	m	Steady	Good	
0928-3	m	Steady	Good	
0930-2	m	Pulsed	Poor	Atypical dynamic forcing
1001-1	m	Steady	Fair	

Note. "Date" and "Stage" are as in Table 1. "Steady/pulsed" refers to whether simulated convection was relatively steady or occurred in discrete pulses. "Quality" refers to the degree to which the simulated mass flux profile agreed with that observed. "Comment" highlights noteworthy aspects of each case.

Based on the satellite loops, these events were classified into growing, mature, and decaying cases. The presence of expanding areas of highly time-dependent active cells indicated growing systems, while their absence and generally increasing IR brightness temperatures indicated decay. Transitions between these two regimes indicated mature systems. The development stages of the selected convective systems are listed in Table 1.

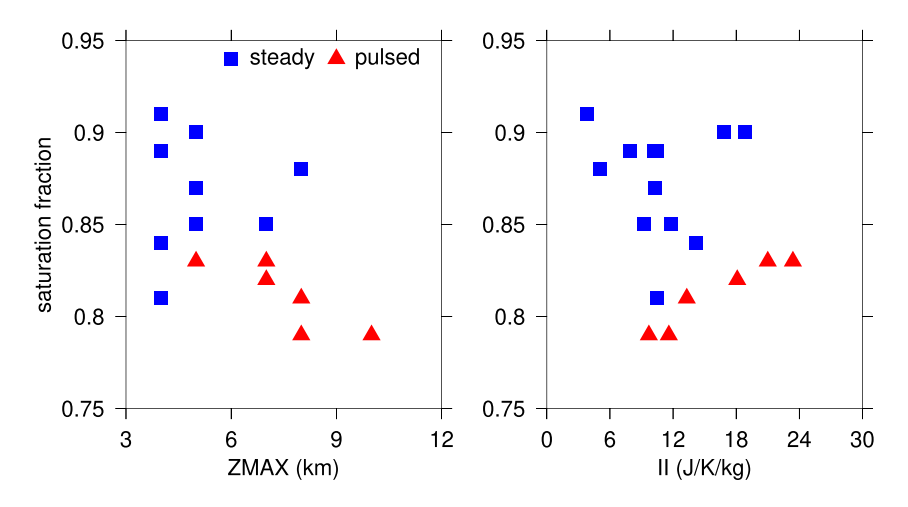


Figure 3. Scatter plots in the SF-ZMAX and SF-II planes of the 18 growing and mature convective cases that showed either steady convection (blue squares) or repeated convective pulsations (red triangles).

RAYMOND ET AL. 6 of 16

19422466, 2024, 3, Downloaded from https

onlinelibrary.wiley.com/doi/10.1029/2023M5003980, Wiley Online Library on [22/03/2025]. See the Terms and Conditions (https://onlinelibrary.wiley.com/terms-and-conditions) on Wiley Online Library for rules of use; OA articles are governed by the applicable Creative Commons Licens

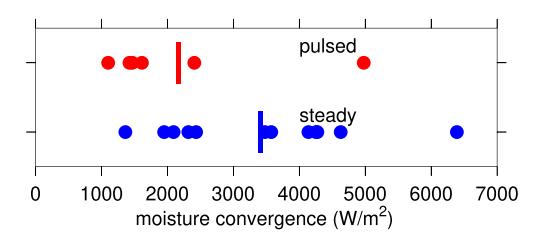


Figure 4. Scatter plot of integrated moisture convergence (Sm) for pulsed (red) and steady (blue) convective cases. The vertical lines indicate mean values of moisture convergence for the two cases.

Though this classification system is somewhat subjective, the observational results from the 3DVar analyses were generally in agreement with the satellite-derived evaluations. In particular, as Figure 1 shows, convection classified as growing was generally found to have negative values of the entropy divergence Se, whereas entropy divergence tended to be positive for systems classified as mature. This is as expected in the discharge-recharge cycles of convection documented by Inoue and Back (2015a, 2015b, 2017) and Masunaga and L'Ecuyer (2014) (Note that these authors used moist static energy rather than moist entropy in their analyses.).

2.2. SWTG Model

The Goconv model described in Raymond and Fuchs-Stone (2021b), updated to version 077, was used here. The physics of this version is the same as in version 071 used in the above paper. A minor addition was made to model initialization code.

As in Raymond and Fuchs-Stone (2021b), $120 \times 120 \times 60$ grid cells are used, with a cell size of $334 \times 334 \times 334$ m, yielding a model domain of approximately $40 \times 40 \times 20$ km. The model time step is 0.75 s and the model is run for 5×10^5 time steps or 3.75×10^5 s (approximately 4.3 days). Fixed radiative cooling of 1 K/day up to 12 km, tapering linearly to zero at 15 km, is used as before. Bulk flux boundary conditions are applied at the surface.

Figure 2 helps explain the different domains used in the SWTG calculations. The convective box coincides with the model domain in which explicit calculations are performed, while the thermodynamic conditions in the reference region represent the surrounding environment and are uniform and fixed by the reference profiles. Air from the reference region is entrained into the convective region and instantly mixed horizontally through the convective box in response to the demands of mass continuity and (optionally) from ventilation by the ambient wind (see discussion below). Corresponding detrainment occurs as well, but is not allowed to modify the reference profile.

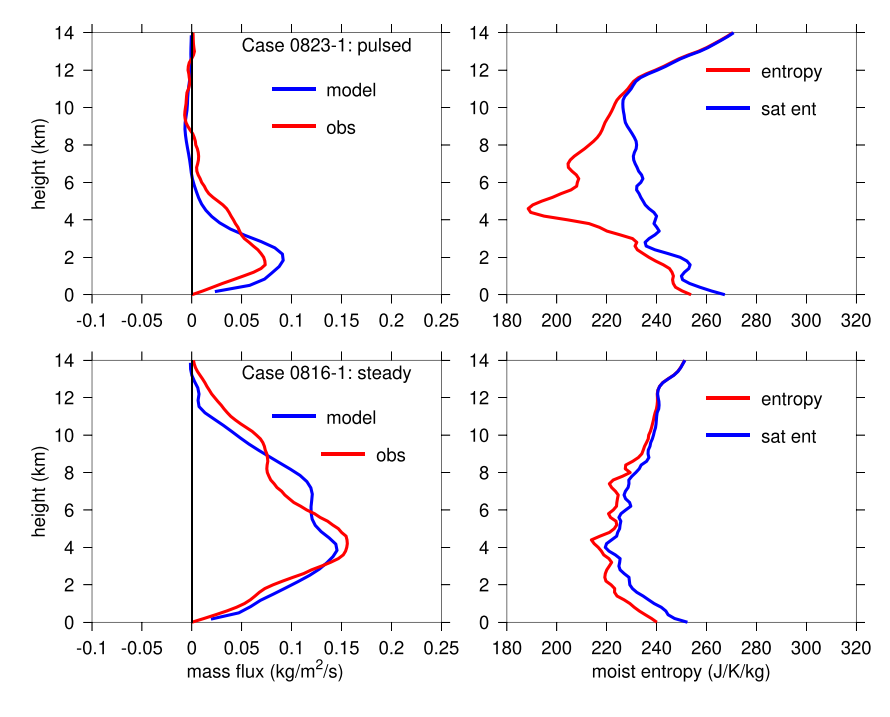


Figure 5. Left panels: Observed and simulated mass flux profiles for two cases, one with pulsed convection (0823-1) and one with steady convection (0816-1). Right panels: Observed vertical profiles of moist entropy and saturated moist entropy for these two cases.

RAYMOND ET AL. 7 of 16

onlinelibrary.wiley.com/doi/10.1029/2023MS003980,

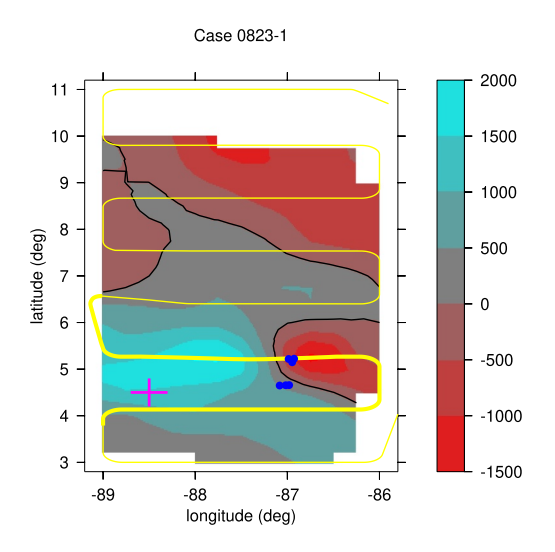


Figure 6. Plan view of the Intertropical Convergence Zone region of OTREC showing the pattern of moisture convergence and the track of the Gulfstream-V aircraft on 23 August 2019. The thick segment of the track line shows the location of the HIAPER Cloud Radar radar particle vertical velocity presented in Figure 8 while the magenta cross indicates the 3DVar sampling location. The blue dots show lightning flashes observed by the GOES-16 Geostationary Lightning Mapper during the interval 13–17 UTC, the approximate period when the Gulfstream-V was in the vicinity of region under consideration.

Physically, we identify the reference region with the clear air outside of the region of concentrated convection. The reference profiles are simply the profiles provided by the 3DVar analysis at the identified location of the convection. Since this analysis is taken from dropsondes mostly deployed outside of the convective region (for flight safety reasons), it is more representative of the convective environment than of the region of intense convection itself, as desired.

The ventilation option in the SWTG code attempts to emulate the effect of storm-relative winds bringing environmental air into close proximity with the convection. This is in addition to the entrainment and detrainment of air into and out of the convective domain required by mass continuity with the weak temperature gradient vertical mass flux. It operates by mixing reference profile air into the convective box in proportion to the reference profile storm-relative wind speed at each level. As used in Raymond and Fuchs-Stone (2021b), it was found to cause inordinate suppression of individual convective cases, unlike the composite cases studied in that paper. This may be due to the small 40 km model domain size used in the computation of the ventilation parameter rather than the more physical observed convective domain, which was typically much larger, where ventilation effects are weaker. For this reason, the ventilation option is turned off in the present simulations

The model output used in this paper is derived from area-averaged time series of the raw output. The averaging cancels out the explicit model flows due to the periodic lateral boundary conditions (with the exception of a small

contribution from sound waves), leaving only the SWTG vertical velocity and the corresponding lateral inflows and outflows. The model variables of particular interest are the area-averaged vertical mass flux (equal to the SWTG vertical velocity times the density) and the area-averaged and vertically integrated horizontal moisture convergence (Equation 6) and horizontal moist entropy divergence (Equation 7). These quantities can be

compared directly with the corresponding observed quantities computed from the 3DVar analyses.

Simulations are initialized with a localized pulse of moist entropy s in the lower troposphere of the form

$$\delta s_{init} = s_0 \exp\left[-r^2/r_0^2 - z/z_0\right]$$
 (9)

where $s_0 = 20$ J/K/kg, r is the horizontal distance from the center of the domain, z is the height above the surface, $r_0 = 2,000$ m, and $z_0 = 1,000$ m. In addition, each entropy field point is perturbed periodically by the addition of a term of the form $\delta s_{random} = Rs_1 \exp(-z/z_0)$ where R varies randomly over the range [-1, 1] and $s_1 = 0.1$ J/K/kg. This has the purpose of countering any tendency of the simulation to settle into a permanent quiescent state, but otherwise has little effect.

Figure 7. Satellite infrared image of OTREC region at 1400 UTC on 23 August 2019. The blue square indicates the location of the mass flux profile and sounding in the 3DVar analysis.

3. Simulation of Growing and Mature Convection

All 20 cases listed as growing or mature convection in Table 1, including 0909-1 which had both growing and decaying components, are simulated, as described above. Cases listed as decaying are not considered further in this paper. Table 2 indicates how successful each simulation was in reproducing the vertical profile of mass flux seen in the 3DVar analysis for each case, with a rating of "poor," "fair" or "good." Good includes all simulations reproducing the observed structure of convection with simulated mass flux values within typically 20% of observation and with the simulated mass flux

RAYMOND ET AL. 8 of 16

19422466, 2024, 3, Downloaded from https://agupubs.onlinelibrary.wiley.com/doi/10.1029/2023MS003980, Wiley Online Library on [22/03/2025]. See the Terms and Conditions (https://agupubs.onlinelibrary.wiley.com/doi/10.1029/2023MS003980, Wiley Online Library on [22/03/2025]. See the Terms and Conditions (https://agupubs.com/doi/10.1029/2023MS003980, Wiley Online Library on [22/03/2025].

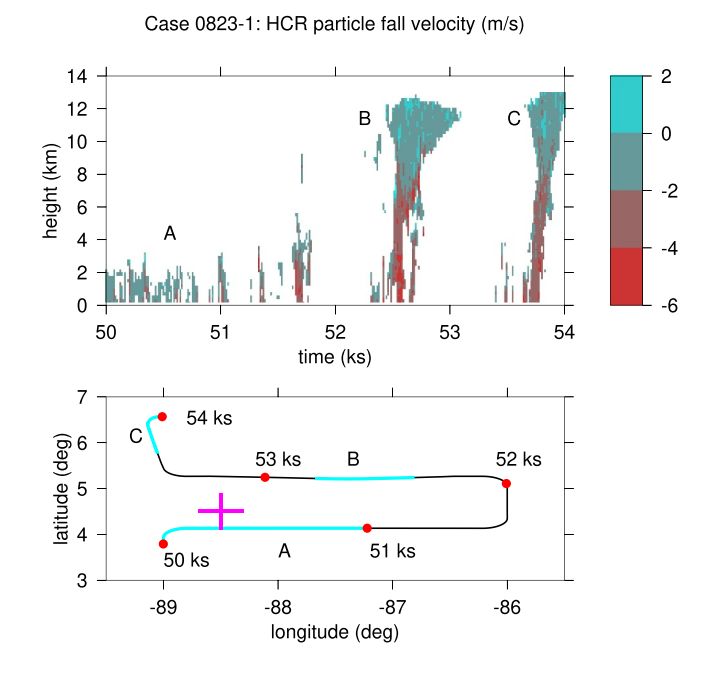


Figure 8. HIAPER Cloud Radar (HCR) radar vertical particle velocity (positive upward) for Case 0823-1 on 23 August 2019 along the thick yellow track segment in Figure 6. Details of various features along this track are shown below the radar plot. The magenta cross marks the location of the mass flux and sounding plots in Figure 5 for this case. Segment A represents shallow convection whereas segments B and C show deep convective regions. Attenuation of the radar beam by overlying hydrometeors is responsible for much of the missing data below 4 km.

maximum within 1-2 km of the observed maximum. Out of the 20 cases, 11 were considered good under these criteria. Simulations not making this cut, but nevertheless having roughly the observed structure and mass flux values within a factor of 2 of observation were considered "fair." Four cases fell into this category. The remaining 5 cases failed both of these criteria and were rated poor.

After an initial equilibration period, most simulations settled into either nearly steady convection or into a series of convective pulses separated by long quiescent periods. Table 2 lists whether each simulation is pulsed or steady. Simulations rated as steady were more likely to be in good agreement with observations than those rated as pulsed. In particular, of the 13 steady cases, 9 of the simulations were rated as good, 2 as fair, and 2 as poor, while for the 5 pulsed cases, 2 were good, 2 were fair, and 1 was poor. Thus, the model has more problems with the dynamic behavior of the pulsed cases than with the more statistically static behavior in the steady cases.

Whether simulated convection is steady or pulsed should in principle be determinable from the initial sounding and the sea surface temperature (SST). Comparison of various variables with the time dependence of convection shows that only the saturation fraction (57%), the instability index (57%), the level of maximum parcel buoyancy (41%), and CAPE (45%) are correlated with this property at the 99% level with the indicated percentage of explained variance. The DCIN, the shear in the lowest 2 km, and the SST show no correlation with it (\leq 3%). The CAPE and the instability index are highly correlated with each other for the 20 growing and mature cases but the instability index shows a somewhat better correlation with pulsation status than does CAPE. The saturation fraction, instability index, and elevation of maximum parcel buoyancy together explain 83% of the variance in pulsation status.

Figure 3 shows scatter plots of saturation fraction versus level of maximum parcel buoyancy and versus instability index for all cases except the two that

produced a single pulse of convection. There is a strong tendency for the steady convective cases to exhibit higher saturation fraction, lower instability index, and lower elevations of maximum parcel buoyancy than the pulsing cases.



Figure 9. Photograph looking north from the Gulfstream-V from its location near $(-89^{\circ}, 4^{\circ})$ at about 1400 UTC.

Figure 4 shows a scatter plot of the moisture convergence of the convective cases with the pulsed cases in red and the steady cases in blue. The outlying pulsed case with moisture convergence near 5,000 W/m² corresponds to Case 0930-2, which exhibited atypical mechanical forcing due to unusual boundary layer flow from the north overriding cooler southerly flow near a latitude of 4°, thus violating the weak temperature gradient approximation used in the simulations. Even including this odd case in the averaging, the average moisture convergence for the steady cases is significantly greater than that for the pulsed cases. Since the precipitation and the moisture convergence are generally the biggest terms in the moisture budget, this confirms that steady cases produce more precipitation on the average than the pulsed cases.

3.1. Two Case Studies

We now investigate the observations for two limiting cases, a case showing pulsed behavior in a numerical simulation (0823-1), and a case which showed steady behavior (0816-1). The soundings and mass flux profiles for these two cases are shown in Figure 5.

Figure 6 shows the track of the Gulfstream-V aircraft on 23 August 2019 for the pulsed case (0823-1), superimposed on a plot of the moisture convergence

RAYMOND ET AL. 9 of 16

agupubs.onlinelibrary.wiley.com/doi/10.1029/2023MS003980, Wiley Online Library on [22/03/2025]. See the Terms'

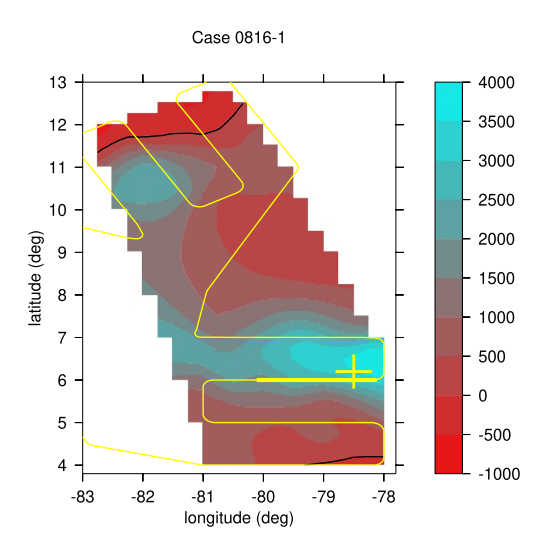


Figure 10. As in Figure 6 except for Colombian coast/Southwest Caribbean on 16 August 2019. The corresponding radar plot is shown in Figure 12. In this case, all lightning in the interval 12–19 UTC is shown.

derived from the 3DVar analysis of the dropsonde data. The magenta cross indicates the location of the mass flux profile and sounding shown in Figure 5.

Figure 7 shows a 2 km resolution IR satellite image for the OTREC study area at 1400 UTC on 23 August 2019 for the pulsed case. The blue square indicates the location of the sounding and mass flux derived from the 3DVar analysis for this case. At that time this region exhibited only shallow convection, as the satellite image indicates. However, isolated deep convective cells near (-87°, 5°) in Figure 7 are producing lightning, as seen in Figure 6.

Figure 8 shows the HCR radar vertical velocity along the thick yellow track shown in Figure 6. Three segments of interest are located by the track detail in the lower panel. Two deep convection segments B and C show precipitation in the isolated deep convective cells noted above. The radar data are useful for distinguishing graupel from ice crystal aggregates above the freezing level near 4.5 km; the aggregates show a distinct increase in fall speed at the freezing level as they rapidly melt, whereas the graupel does not. Examination of Figure 8 shows no signs of a velocity discontinuity at the freezing level, indicating that most precipitation above the freezing level was in the form of graupel. Note that the shallow convection in segment A returned a significant radar echo, indicating that it was producing precipitation.

The photograph in Figure 9 shows both the deep convection near $(-89^{\circ}, 6^{\circ})$ and the shallow convection nearer the aircraft. The latter is likely associated with the region of moisture convergence seen in Figure 6 and the shallow mass flux profile seen in the upper panel of Figure 5.

We now present analogous results for the steady case (0816-1). Figure 10 shows a plan view of the aircraft track and moisture convergence pattern for this case on 16 August 2019. The sounding and mass flux profile are located in a region of strong moisture convergence. Unlike the 0823-1 case, no lightning for the entire flight interval of the Gulfstream-V was found near the observed convection.

Figure 11 shows the IR satellite image for the steady case. A bottom-heavy mass flux profile as seen in the lower panel of Figure 5 exists throughout the region of strong moisture convergence and largely coincides with the large

but unspectacular convective cluster seen off of the Pacific coast of Colombia in Figure 11.

The HCR particle vertical velocity pattern for 0816-1 is shown in Figure 12. Unlike the 0823-1 case, ice crystal aggregates are mostly seen above the freezing level. With the exception of a region toward the right end of the plot, which is near the east end of the convective system according to Figures 10 and 11, the predominance of aggregates is indicated by the strong jump in particle velocity near the freezing level at approximately 4.5 km. However, unlike many cases where this pattern indicates a stratiform rain situation, the mass flux profiles uniformly exhibit bottom-heavy convection in this region, as shown in Figure 5 for this case. As the aircraft passed directly over the heart of this convective system, it is unlikely that extensive regions of graupel formation existed, aside from that seen at its east end. Thus, the system appeared to consist mostly of deep but bottom-heavy convection that produced precipitation above the freezing level mainly in the form of ice crystal aggregates.

SUEETS 2019/02/15 EXPUID DIS COST COLT SOCIETY OF THE PROPERTY OF THE PROPERTY

Figure 11. As in Figure 7 except for 1500 UTC on 16 August 2019. The blue square locates the 3DVar sounding and mass flux profile.

3.2. SWTG Simulations of the Two Cases

We now illustrate the difference between pulsed and steady convective systems in SWTG simulations of the two limiting cases. Figure 13 shows the simulated vertical mass flux as a function of time and height for the two cases. The pulsed case exhibits convective pulses at intervals of slightly greater than one day, which start with gradually intensifying shallow convection followed by a short but intense period of deep convection that decays rapidly. In

RAYMOND ET AL. 10 of 16

1942/2666, 2024, 3, Downloaded from https://gupubs.onlinelibrary.wiley.com/doi/10.1029/2023MS003980, Wiley Online Library on [22/03/2025]. See the Terms and Conditions (https://onlinelibrary.wiley.com/terms-and-conditions) on Wiley Online Library for rules of use; OA articles are governed by the applicable Creative Commons Licens

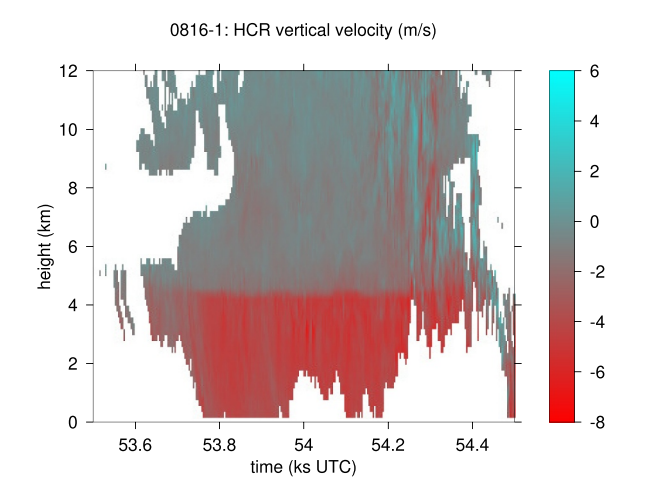


Figure 12. As in Figure 8 except for Case 0816-1 on 16 August 2019. The Gulfstream-V track segment for this figure is shown in Figure 10.

contrast, the steady case intensified monotonically and then undergoes only small oscillations.

Figure 5 shows observed and simulated mass flux profiles and thermodynamic soundings at times indicated in Figure 13 for these two cases. Note that the simulated mass flux displayed for the pulsed case is taken from the growing phase of the initial pulse as indicated in Figure 13. The simulated mass flux for the steady case is a time average starting when the simulation reaches a steady state.

Though surface thermodynamic conditions for the above two cases are similar, the thermodynamic profiles of the two cases differ dramatically aloft. In particular, the mid-level humidity is much lower for the pulsed case, as evidenced by the large separation between the moist and saturated moist entropies, and the instability index is larger (see Table 1). The minimum in saturated moist entropy is also at a much higher elevation for the pulsed case, indicating that the level of maximum parcel buoyancy is higher.

Many observed convective systems in the tropical regions undergo time evolution characterized by a cycle in the GMS plane of Inoue and

Back (2017); see also Inoue and Back (2015a, 2015b), Masunaga and L'Ecuyer (2014). In this plane the moisture convergence (or dry static stability divergence) is plotted against the moist static stability (or moist entropy) divergence. In the growing phase of the system the moist entropy divergence tends to be negative with increasing, positive moisture convergence. The entropy divergence then becomes positive, followed thereafter by peak and then decreasing moisture convergence.

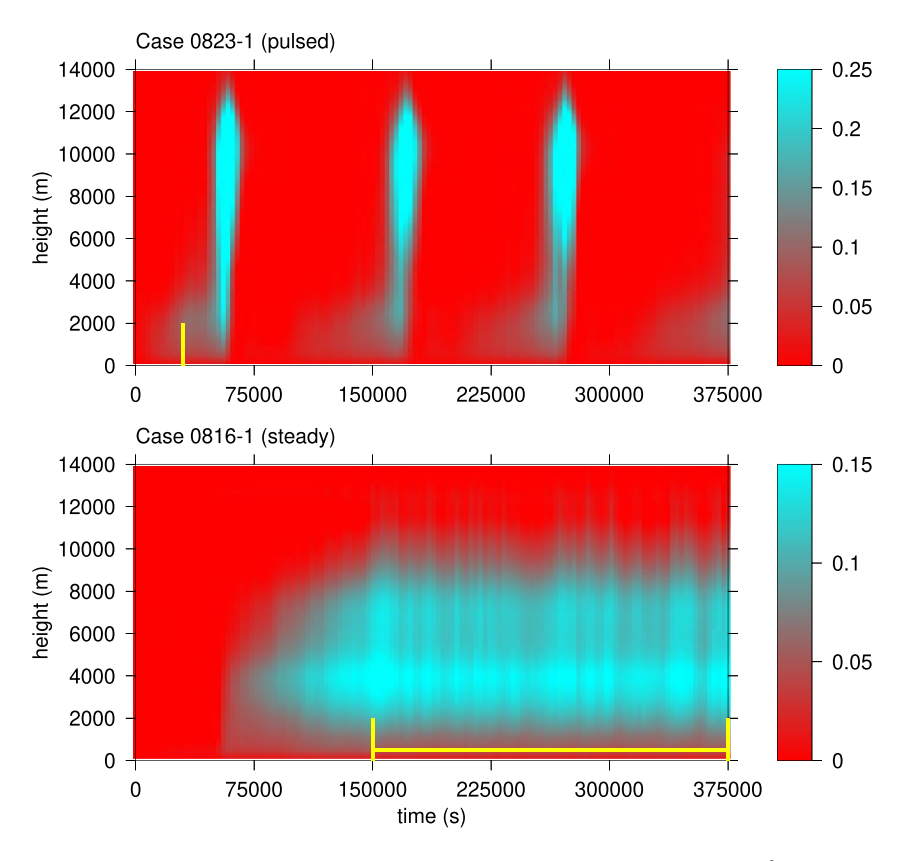


Figure 13. Shaded plots of computed vertical mass flux as a function of time and height (units: $kg/m^2/s$) for cases 0823-1 and 0816-1. The vertical yellow bars show the times for the corresponding mass flux profiles shown in Figure 5. For 0816-1, the averaging period for the plotted mass flux is shown.

RAYMOND ET AL.

19422466, 2024, 3, Downloaded from https:

/agupubs.onlinelibrary.wiley.com/doi/10.1029/2023MS003980, Wiley Online Library on [22/03/2025]. See the Terms and Conditions (https://onlinelibrary.wiley.com/terms-and-conditions) on Wiley Online Library for rules of use; OA articles are governed by the applicable Creative Commons Licens

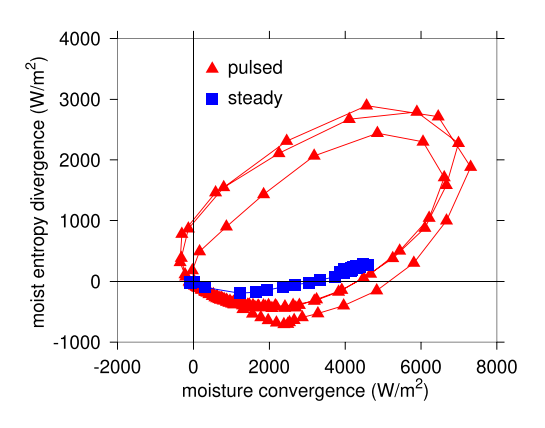


Figure 14. Evolution of the pulsed Case 0823-1 (red triangles) and the steady Case 0816-1 (blue squares) in the gross moist stability plane. Smoothing with a 3,000 s smoothing length was used to reduce noise. The time between triangles is 2,250 and 9,000 s for squares.

The simulated convection of all cases listed in Table 2 as pulsed undergo oscillations in the GMS plane as described above. However, those listed as steady do not. Figure 14 shows the time evolution of 0816-1 and 0823-1 for the full 375 ks integration time in the GMS plane. The pulsed case shows multiple cycles exhibiting the above-described evolution in the GMS plane whereas the steady case reaches a near-steady state with only small oscillations.

Both cases shown in Figure 14 begin with negative values of moist entropy divergence (and hence negative GMS) and transition to positive values. However, the excursions of moist entropy divergence are much smaller in the steady convection case than in the pulsed case.

4. Discussion

Our analysis of 20 growing and mature convective regions shows a spectrum of convective characteristics from cases with lower column humidity, higher instability, graupel above the freezing level, and pulsing behavior in SWTG simulations, versus those with higher humidity, lower instability, aggregates,

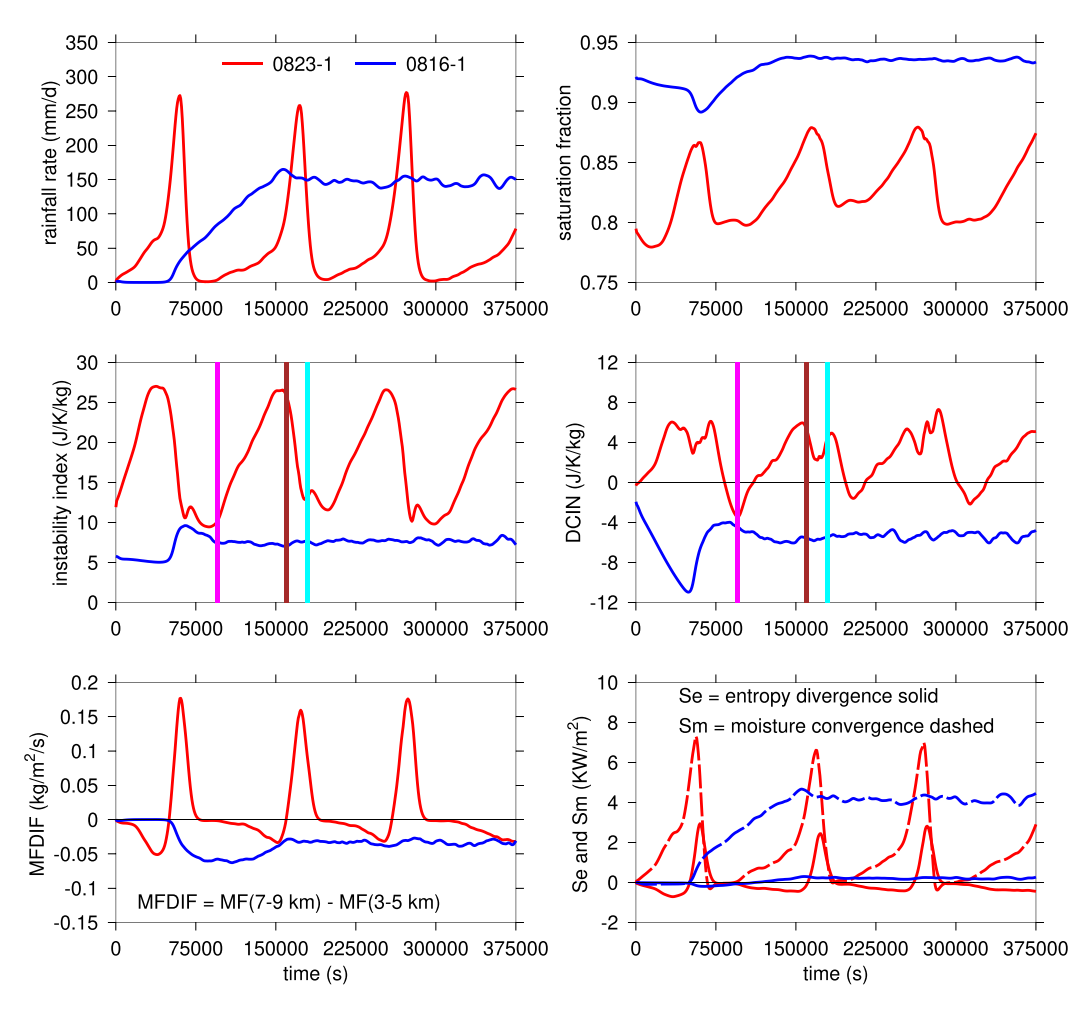


Figure 15. Time series of rainfall rate (estimated from the moisture convergence), saturation fraction, deep convective inhibition (DCIN), instability index, difference between the mass fluxes in the 7–9 km and 3–5 km layers (MFDIF), and the entropy divergence (solid lines) and moisture convergence (dashed lines) for the showers (0823-1; red) and rains (0816-1; blue) cases. A smoothing filter with a smoothing length of 3,000 s is applied. The magenta, brown, and cyan vertical lines in the instability index and DCIN plots indicate the times of sounding plots for the showers case in Figure 16.

RAYMOND ET AL. 12 of 16

19422466, 2024, 3, Downloaded from https://agupubs.onlinelibrary.wiley.com/doi/10.1029/2023MS003980, Wiley Online Library on [22/03/2025]. See the Terms and Conditions (https://or

and-conditions) on Wiley Online Library for rules of use; OA articles are governed by the applicable Creative Commons Licenso

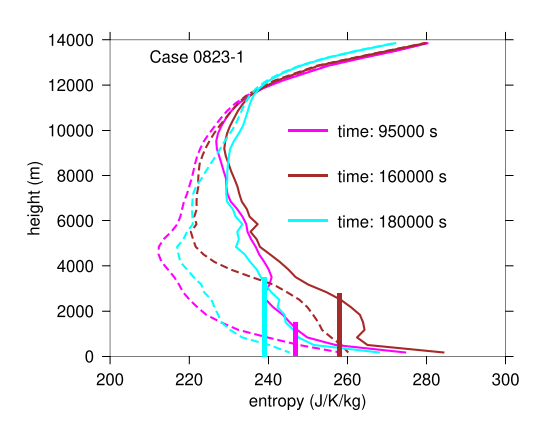


Figure 16. Soundings for the showers case showing the moist entropy (dashed curve of each color) and the saturated moist entropy (solid curve) at three different times, indicated by the vertical lines of the corresponding colors in the instability index and deep convective inhibition plots of Figure 15. The thick vertical lines in this plot show the moist entropies of parcels lifted moist adiabatically from the lowest kilometer. The intersections with the corresponding saturated moist entropy sounding curves indicate the levels of free convection for the three soundings.

and steady behavior in simulations. We identify the former as belonging to Ramage's showers regime and the latter belonging to the rains regime. As Ramage notes, a continuous spectrum from one regime to the other exists. However, to emphasize the differences between the two regimes, two extreme cases were chosen for analysis in the previous section, exemplifying the showers and rains regimes respectively. We now attempt to understand why this divergent behavior between the two regimes occurs.

Figure 15 presents time series plots that summarize the differences between the simulations of the showers (0823-1; red) and rains (0816-1; blue) cases. The definitions of the parameters are given in Section 2.1.

The sequence of events leading to the suppression of convection at the end of a pulse in the showers case is somewhat complex. The magenta, brown, and cyan vertical lines in the instability index and DCIN plots in Figure 15 indicate the times of the 3 thermodynamic soundings shown in Figure 16. The magenta sounding represents conditions at the beginning of the second pulse shown in Figure 15. This sounding is favorable to convection, with a level of free convection (LFC) of about 1,500 m, and with precipitation beginning at this time. Both the instability index and the DCIN reach their minimum values then.

The brown sounding is taken just before the maximum in precipitation and just after the maxima in instability index and DCIN. The increase in moist entropy

between 1,000 and 5,000 m in this sounding is likely the result of detrainment of moist air by the initial surge of shallow, bottom-heavy convection. This layer of air is very unstable and likely the origin of large, ascending thermals that form the subsequent burst of deep, top-heavy convection. However, the associated development of a strong inversion starting near 1,000 m in the brown sounding increases the LFC of surface air to 2,700 m and cuts off these thermals from boundary layer air at that point. This is reflected in the large positive value of DCIN.

The ascent of the above thermals ultimately results in the cyan sounding, which resembles the original magenta sounding with the exception that a cold pool has formed below 2,000 m from descending, evaporatively cooled air, causing the LFC to rise to 3,500 m. The recovery of the boundary layer by surface heat and moisture fluxes ultimately returns the atmosphere to an unstable state, at which point subsequent convection is formed. The above cycle appears to be responsible for the pulsating nature of the convection in the simulation and is illustrated by the evolution in the GMS plane of the pulsed case in Figure 14.

The rains case appears to avoid this mechanism by virtue of a sounding (see Figure 5) with high saturation fraction, low DCIN, and low instability index. The low value of DCIN facilitates the development of deep convective updrafts directly from the boundary layer, without the complex mechanisms acting in the showers case. Furthermore, the high humidity and the low instability index together result in downdrafts with less negative buoyancy than in the showers case, weakening the flow of low moist entropy air into the boundary layer and the

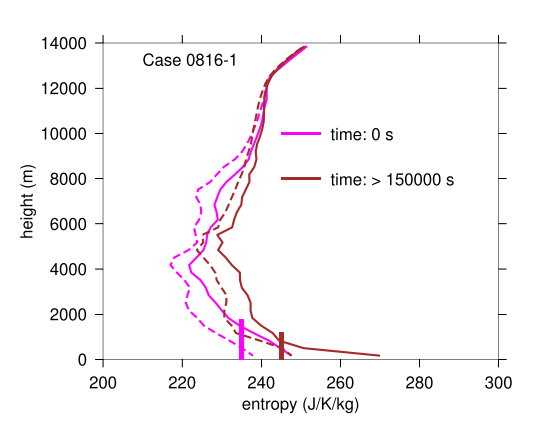


Figure 17. As in Figure 16 except for initial (magenta) and time-mean (brown) soundings for the rains case.

corresponding formation of a cold pool. Finally, the low elevation of the minimum in saturated moist entropy in the sounding (4 km as opposed to 10 km for the showers case) results in deceleration of ascending air above the 4 km level which likely reduces the tendency of compensating subsidence to form a strong inversion at low levels. The result of attenuation of mechanisms acting to suppress follow-on convection in the showers case allows convection to develop more or less continuously in the rains case. Though peak values of rainfall rate are greater in the showers case, the time-averaged rainfall in the rains case is actually three times that occurring in the showers case.

Figure 17 shows the initial sounding derived from the 3DVar analysis and the mean sounding for the steady phase of the rains case starting at 150,000 s. The mean sounding is somewhat warmer and more moist with less convective inhibition than the initial sounding. However, overall the mean sounding is not so different in character from the initial sounding.

RAYMOND ET AL. 13 of 16

19422466, 2024, 3, Downloaded from https

agupubs.onlinelibrary.wiley.com/doi/10.1029/2023MS003980, Wiley Online Library on [22/03/2025]. See the Terms and Conditi

Table 3Characteristics of Showers (0823-1) and Rains (0816-1) Simulations

Variable	Showers case	Rains case
CAPE (J/kg)	1,036	294
Saturation fraction	0.79	0.91
Lightning	Yes	No
Ice type	Graupel	Mostly aggregates
Rain type	Intense, episodic	Moderate, continuous
Mean rain rate (mm/day)	53	148
Mean mass flux 4 km (kg/m²/s)	0.020	0.097
Instability index (J/K/kg)	9.7	3.8
DCIN (J/K/kg)	-0.7	-2.9
Level max buoyancy (km)	10	4

Note. The 4 km mass flux was averaged over a $2^{\circ} \times 2^{\circ}$ square centered at $(-88^{\circ}, 5^{\circ})$ for 0823-1 and $(-79^{\circ}, 6^{\circ})$ for 0816-1 and represents the convergence in the lowest 4 km.

In both cases the evolution of convection begins with the gradual increase in the intensity of a region of convection with bottom-heavy mass fluxes. In the showers case this is followed by the eruption of a large thermal that forms from the moistened air in the lowest 3–4 km provided by the bottom-heavy convection. In the rains case the development of such strong transient thermals is thwarted by the factors discussed above, namely the high saturation fraction, the low value of instability index (and correspondingly, CAPE), and the low elevation of maximum parcel buoyancy.

5. Conclusions

Table 3 summarizes the characteristics of the showers and rains cases pertinent to Ramage (1971) and Williams et al. (1992). In particular, the conditional instability is much greater in the showers case than in the rains case whereas the humidity is significantly less. The showers case exhibited lightning while the rains case did not. The mean rainfall rate and vertical mass flux were greater in the rains case, while both the DCIN and the elevation of maximum parcel buoyancy were both greater in the showers case. All of Ramage's and Williams et al.'s distinguishing conditions between rains and showers except that of vertical wind shear are satisfied. The difference in the

wind profiles was not particularly large. We therefore propose that Ramage's rains regime is produced by environments exhibiting the characteristics associated with steady convection in our model simulations, whereas the showers regime occurs when these conditions are violated.

The two cases discussed in detail here are clearly limiting cases and as Ramage indicated, there exists a distribution in characteristics between these limits. However, the clear separation of the 18 cases in Figure 3 indicates that the categorization suggested by our two limiting studies appears to be generally useful. It highlights a qualitative change in the characteristics of convection as the environment becomes more moist and more stable. In particular, convective mass fluxes become more bottom-heavy, mean rainfall rate increases even as maximum rainfall rates decrease, and the stratiform-cold pool phase of showery convection decreases or disappears. These changes result in major changes in the feedback of convection on the atmosphere as well.

Data Availability Statement

The 3DVar analyses used in this paper are available at Raymond (2021b). This analysis utilized our Candis data analysis software, which is archived at Raymond (2021a). Two kilometer GOES-16 infrared satellite images for OTREC are archived at NCAR-EOL (2019b). HCR radar data may be obtained atr data NCAR-EOL (2019a). GOES-16 Geostationary Lightning Mapper data are available at NOAA (2023). Source code and documentation for version 077 of the Goconv cloud model may be found at Raymond (2023a) and model output for this paper resides at Raymond (2023b). Documentation on the construction of figures appears at Raymond (2023c).

Acknowledgments

We thank the Earth Observing Laboratory of the National Center for Atmospheric Research for their excellent support of the OTREC project. We also thank Eric DeWeaver of the National Science Foundation for his wisdom in guiding us through a complex field program. Larissa Back, two anonymous reviewers, and the Editor Tapio Schneider provided excellent feedback, for which we thank them. This work was supported by National Science Foundation Grant 2034817.

References

Back, L. E., & Bretherton, C. S. (2009a). On the relationship between SST gradients, boundary layer winds, and convergence over the tropical oceans. *Journal of Climate*, 22(15), 4182–4196. https://doi.org/10.1175/2009jcli2392.1

Back, L. E., & Bretherton, C. S. (2009b). A simple model of climatological rainfall and vertical motion patterns over the tropical oceans. *Journal of Climate*, 22(23), 6477–6497. https://doi.org/10.1175/2009jcli2393.1

Back, L. E., Hansen, Z., & Handlos, Z. (2017). Estimating vertical motion profile top-heaviness: Reanalysis compared to satellite-based observations and stratiform rain fraction. *Journal of the Atmospheric Sciences*, 74(3), 855–864. https://doi.org/10.1175/jas-d-16-0062.1

Bretherton, C. S., Peters, M. E., & Back, L. E. (2004). Relationships between water vapor path and precipitation over the tropical oceans. *Journal of Climate*, 17(7), 1517–1528. https://doi.org/10.1175/1520-0442(2004)017<1517:rbwvpa>2.0.co;2

Byers, H. R., & Braham, R. R. (1948). Thunderstorm structure and circulation. *Journal of Meteorology*, 5(3), 71–86. https://doi.org/10.1175/1520-0469(1948)005<0071:tsac>2.0.co:2

Elsberry, R. L., & Harr, P. A. (2008). Tropical cyclone structure (TCS08) field experiment science basis, observational platforms, and strategy. Asia-Pacific Journal of Atmospheric Sciences, 44, 209–231.

Fuchs, Ž., & Raymond, D. J. (2002). Large-scale modes of a nonrotating atmosphere with water vapor and cloud-radiation feedbacks. *Journal of the Atmospheric Sciences*, 59(10), 1669–1679. https://doi.org/10.1175/1520-0469(2002)059<1669:lsmoan>2.0.co;2

Fuchs-Stone, Ž., Raymond, D. J., & Sentić, S. (2020). OTREC2019. Convection over the East Pacific and Southwest Caribbean. Geophysical Research Letters, 47(11), e2020GL087564. https://doi.org/10.1029/2020GL087564

RAYMOND ET AL. 14 of 16

- Gjorgjievska, S., & Raymond, D. J. (2014). Interaction between dynamics and thermodynamics during tropical cyclogenesis. *Atmospheric Chemistry and Physics*, 14(6), 3065–3082. https://doi.org/10.5194/acp-14-3065-2014
- Herman, M. J., & Raymond, D. J. (2014). WTG cloud modeling with spectral decomposition of heating. Journal of Advances in Modeling Earth Systems, 6(4), 1121–1140. https://doi.org/10.1002/2014MS000359
- Houze, R. A. (1981). Structures of atmospheric precipitation systems: A global survey. *Radio Science*, 16(5), 671–689. https://doi.org/10.1029/rs016i005p00671
- Houze, R. A. (1997). Stratiform precipitation in regions of convection: A meteorological paradox. *Bulletin America Meteorology Social*, 78(10), 2179–2196. https://doi.org/10.1175/1520-0477(1997)078<2179:spiroc>2.0.co;2
- Houze, R. A. (2004). Mesoscale convective systems. Reviews of Geophysics, 42(4), RG4003. https://doi.org/10.1029/2004RG000150
- Houze, R. A., & Betts, A. K. (1981). Convection in gate. Reviews of Geophysics and Space Physics, 19(4), 541–574. https://doi.org/10.1029/ rg019i004p00541
- Houze, R. A., Rasmussen, K. L., Zuluaga, M. D., & Brodzik, S. R. (2015). The variable nature of convection in the tropics and subtropics: A legacy of 16 years of the Tropical Rainfall Measuring Mission satellite. Reviews of Geophysics, 53(3), 994–1021. https://doi.org/10.1002/2015RG000488
- Inoue, K., & Back, L. (2015a). Column-integrated moist static energy budget analysis on various time scales during TOGA COARE. Journal of the Atmospheric Sciences, 72(5), 1856–1871. https://doi.org/10.1175/jas-d-14-0249.1
- Inoue, K., & Back, L. E. (2015b). Gross moist stability assessment during TOGA COARE: Various interpretations of gross moist stability. Journal of the Atmospheric Sciences, 72(11), 4148–4166. https://doi.org/10.1175/jias-d-15-0092.1
- Inoue, K., & Back, L. E. (2017). Gross moist stability analysis: Assessment of satellite-based products in the GMS plane. Journal of the Atmospheric Sciences, 74(6), 1819–1837. https://doi.org/10.1175/jas-d-16-0218.1
- Johnson, R. H., & Chang, C.-P. (2007). Winter MONEX. Bulletin America Meteorology Social, 88, 385-388.
- Mapes, B., & Houze, R. A., Jr. (1993). An integrated view of the 1987 Australian monsoon and its mesoscale convective systems, II: Vertical structure. Quarterly Journal of the Royal Meteorological Society, 119(512), 733–754. https://doi.org/10.1256/smsqj.51206
- Mapes, B., & Houze, R. A., Jr. (1995). Diabatic divergence profiles in western Pacific mesoscale convective systems. *Journal of the Atmospheric Sciences*, 52(10), 1807–1828. https://doi.org/10.1175/1520-0469(1995)052<1807:ddpiwp>2.0.co;2
- Masunaga, H., & L'Ecuyer, T. S. (2014). A mechanism of tropical convection inferred from observed variability in the moist static energy budget. Journal of the Atmospheric Sciences, 71(10), 3747–3766. https://doi.org/10.1175/jas-d-14-0015.1
- Montgomery, M. T., Davis, C., Dunkerton, T., Wang, Z., Velden, C., Torn, R., et al. (2012). The pre-depression investigation of cloud systems in the tropics (PREDICT) experiment. *Bulletin America Meteorology Social*, 93(2), 153–172. https://doi.org/10.1175/bams-d-11-00046.1
- NCAR-EOL. (2019a). Hiaper Cloud Radar data for the OTREC project [Dataset]. NCAR EOL. Retrieved from https://catalog.eol.ucar.edu/otrec/
- NCAR-EOL. (2019b). JPEG 2 km infrared satellite images for OTREC project. NCAR EOL. Retrieved from https://catalog.eol.ucar.edu/otrec/satellite
- NOAA. (2023). NOAA GOES16 Geostationary Lightning Mapper (GLM) data [Dataset]. NOAA. Retrieved from https://www.avl.class.noaa.gov/saa/products/search?datatype_family=GRGLMPROD
- Petersen, W. A., Cifelli, R., Boccippio, D. J., Rutledge, S. A., & Fairall, C. (2003). Convection and easterly wave structures observed in the eastern Pacific warm pool during EPIC-2001. *Journal of the Atmospheric Sciences*, 60(15), 1754–1773. https://doi.org/10.1175/1520-0469(2003) 060<1754:caewso>2.0.co:2
- Ramage, C. S. (1971). Monsoon meteorology. Academic Press.
- Raymond, D. J. (2021a). Candis analysis and display software [Software]. Zenodo. https://doi.org/10.5281/zenodo.5150519
- Raymond, D. J. (2021b). 3DVar analyses of dropsondes for OTREC project [Dataset]. Zenodo. https://doi.org/10.5281/zenodo.5152171
- Raymond, D. J. (2023a). Source code and documentation for version 077 of the Goconv cloud model [Software]. Zenodo. https://doi.org/10.5281/zenodo.8253634
- Raymond, D. J. (2023b). Model output for studies of growing and mature convection observed in OTREC. Zenodo. https://doi.org/10.5281/zenodo.8264462
- Raymond, D. J. (2023c). Figure documentation for studies of growing and mature convection observed in OTREC. Zenodo. https://doi.org/10.5281/zenodo.8267486
- Raymond, D. J., Esbensen, S. K., Paulson, C., Gregg, M., Bretherton, C. S., Petersen, W. A., et al. (2004). EPIC2001 and the coupled ocean-atmosphere system of the tropical east Pacific. Bulletin America Meteorology Social, 85(9), 1341–1354. https://doi.org/10.1175/bams-85-9-1341
- Raymond, D. J., & Fuchs, Ž. (2007). Convectively coupled gravity and moisture modes in a simple atmospheric model. *Tellus*, 59A(5), 627–640. https://doi.org/10.1111/j.1600-0870.2007.00268.x
- Raymond, D. J., & Fuchs-Stone, Ž. (2021a). Emergent properties of convection in OTREC and PREDICT. Journal of Geophysical Research: Atmospheres, 126(4), e2020JD033585. https://doi.org/10.1029/2020JD033585
- Raymond, D. J., & Fuchs-Stone, Ž. (2021b). Weak temperature gradient modeling of convection in OTREC. *Journal of Advances in Modeling Earth Systems*, 13(10), e2021MS002557. https://doi.org/10.1029/2021MS002557
- Raymond, D. J., Raga, G. B., Bretherton, C. S., Molinari, J., López-Carrillo, C., & Fuchs, Ž. (2003). Convective forcing in the intertropical convergence zone of the eastern Pacific. *Journal of the Atmospheric Sciences*, 60(17), 2064–2082. https://doi.org/10.1175/1520-0469(2003)
- Raymond, D. J., Sessions, S., Sobel, A., & Fuchs, Ž. (2009). The mechanics of gross moist stability. *Journal of Advances in Modeling Earth Systems*, 1(#9), 20. https://doi.org/10.3894/james.2009.1.9
- Sentic, S., Bechtold, P., Fuchs-Stone, Z., Rodwell, M., & Raymond, D. J. (2022). On the impact of dropsondes on the ECMWF Integrated Forecasting System model (CY47R1) analysis of convection during the OTREC (Organization of Tropical East Pacific Convection) field campaign. *Geoscientific Model Development*, 15(8), 3371–3385. https://doi.org/10.5194/gmd-15-3371-2022
- Sherwood, S. C. (1999). Convective precursors and predictability in the tropical western Pacific. *Monthly Weather Review*, 127(12), 2977–2991. https://doi.org/10.1175/1520-0493(1999)127<2977:cpapit>2.0.co;2
- Sobel, A. H., Yuter, S. E., Bretherton, C. S., & Kiladis, G. N. (2004). Large-scale meteorology and deep convection during TRMM KWAJEX. Monthly Weather Review, 132(2), 422–444. https://doi.org/10.1175/1520-0493(2004)132<0422:lmadcd>2.0.co;2
- Vivekanandan, J., Ellis, S., Tsai, P., Loew, E., Lee, W.-C., Emmett, J., et al. (2015). A wing pod-based millimeter wavelength airborne cloud radar. Geoscientific Instrumentation, Methods and Data Systems, 4(2), 161–176. https://doi.org/10.5194/gi-4-161-2015

RAYMOND ET AL. 15 of 16



Journal of Advances in Modeling Earth Systems

- 10.1029/2023MS003980
- Wang, S., Sobel, A. H., & Nie, J. (2015). Modeling the MJO in a cloud-resolving model with parameterized large-scale dynamics: Vertical structure, radiation, and horizontal advection of dry air. *Journal of Advances in Modeling Earth Systems*, 8(1), 121–139. https://doi.org/10.1002/2015MS000529
- Webster, P. J., & Lukas, R. (1992). TOGA COARE: The TOGA coupled ocean-atmosphere response experiment. *Bulletin America Meteorology Social*, 73(9), 1377–1416. https://doi.org/10.1175/1520-0477(1992)073<1377:tctcor>2.0.co;2
- Williams, E. R., Rutledge, S. A., Geotis, S. G., Renno, N., Rasmussen, E., & Rickenbach, T. (1992). A radar and electrical study of tropical "hot towers". *Journal of the Atmospheric Sciences*, 49(15), 1386–1395. https://doi.org/10.1175/1520-0469(1992)049<1386:araeso>2.0.co;2
- Zipser, E. J. (1969). The role of organized unsaturated convective downdrafts in the structure and rapid decay of an equatorial disturbance. *Journal of Applied Meteorology*, 8(5), 799–814. https://doi.org/10.1175/1520-0450(1969)008<0799:troouc>2.0.co;2
- Zipser, E. J. (1970). The Line Islands experiment, its place in tropical meteorology and the rise of the fourth school of thought. *Bulletin America Meteorology Social*, 51(12), 1136–1146. https://doi.org/10.1175/1520-0477-51.12.1136

RAYMOND ET AL. 16 of 16